2009 IEEE International Conference on Robotics and Automation
Kobe International Conference Center
Kobe, Japan, May 12-17, 2009

Visual Homing for Undulatory Robotic Locomotion

G. López-Nicolás[1], M. Sfakiotakis[2], D. P. Tsakiris[2], A. A. Argyros[2], C. Sagüés[1] and J.J. Guerrero[1]

Abstract— **This paper addresses the problem of vision-based closed-loop control for undulatory robots. We present an image-based visual servoing scheme, which drives the robot to a desired location specified by a target image, without explicitly estimating its pose. Instead, the control relies on the computation of the epipolar geometry between the current and target images. We analyze controllability and stability of the proposed control scheme, which is validated by simulation studies using the SIMUUN computational tools. Preliminary experiments, involving the Nereisbot undulatory robotic prototype, are also presented.**

I. INTRODUCTION

Autonomous navigation of mobile robots is a complex problem that has attracted the attention of the research community during the last decades. Most mobile robots are wheeled vehicles and they have been extensively studied in the literature. Currently, emerging applications demand mobile robots capable of performing autonomous tasks in rugged terrains that are inaccessible to wheeled vehicles: demining, urban search and rescue, etc. Nature has solved the task of locomotion in many ways for a broad range of environments by sliding, burrowing, flying or swimming. Particularly, undulatory locomotion is utilized by many organisms like worms, snakes and fishes to navigate successfully in quite different terrains like water, mud, sand or rugged surfaces. In undulatory locomotion, net displacements are generated through the coupling of the mechanism's internal shape changes to external motion constraints [1], [2], [3].

Many undulatory robots rely on passive wheels to carry out serpentine locomotion [1], [2], [4]. Undulatory prototypes without wheels, which crawl on their underside (see [5], [6] and references therein), or swim (e.g., [3]), are also being developed. The undulatory robotics literature has mainly focused, so far, on mechanical design, modelling and gait generation. However, limited contributions have been presented using sensor-based control schemes performing navigation tasks. Control schemes implementing reactive centering and swarming behaviors for undulatory robots, based on distance sensor data, are described by some of the authors of the present work in [7]. The use of tactile sensors, infrared sensors, cameras and lasers for inspection tasks by snake robots is presented in [8], [9]. Other examples include schemes for map-building and obstacle avoidance [10] or light-following behaviors [11].

Fig. 1. The Nereisbot undulatory robotic prototype, with an on-board camera mounted on its head link.

Vision is one of the most studied sensory modalities for navigation purposes, primarily because it provides rich information of the environment [12]. Visual servoing methods can be classified, depending on how the image data are used, as image-based [13]–[15], position-based [16], [17] and hybrid or partitioned methods [18]–[20]. The framework of the approach presented in this paper is a vision system consisting of a fixed camera mounted on the head of an undulatory robotic locomotor (Fig. 1). The visual control task uses the classical idea of homing in which the desired locations are defined by target images taken previously at those locations by the same or other robot. In [16] a pioneering approach for visual homing was presented based on the epipolar geometry. Several works have developed this idea of using the epipolar geometry in the control loop [21]–[23]. However, these approaches are intended for conventional wheeled mobile robots. In this paper, we propose an image-based control scheme, based on the epipolar geometry, that deals with the particularities of undulatory locomotion. To our knowledge, this is the first visual servoing scheme to demonstrate autonomous navigation of an undulatory robotic system to the target location by relying purely in visual information.

The proposed control scheme is validated by simulations, carried out with the SIMUUN (SIMUlator for UNdulatory locomotion) computational tools [24]. Preliminary experiments are also presented, involving Nereisbot, an undulatory robotic prototype developed at ICS-FORTH [5]–[7], which is equipped with a forward-looking camera (Fig. 1).

The remainder of this paper is structured as follows. Section II gives the modelling of the system. The control scheme is presented in Section III. Controllability and stability analysis are provided in Sections IV and V respectively. The experimental evaluation is presented in Section VI.

This work was supported by "Programa Europa XXI de la Comisión Mixta Caja de Ahorros de la Inmaculada - CONAI+D del Gobierno de Aragón" and projects DPI2006-07928, IST-1-045062-URUS-STP, EU projects VECTOR (FP6-033970) and OCTOPUS (FP7-231608).

[1]DIIS - I3A, Universidad de Zaragoza, Spain.
{gonlopez, csagues, jguerrer}@unizar.es
[2]ICS, FORTH. Heraklion, Crete, Greece. M. Sfakiotakis is also with Electrical Engineering Dept., Technological Educational Institute of Crete. A.A. Argyros is also with the Computer Science Dept., University of Crete.
{sfakios, tsakiris, argyros}@ics.forth.gr

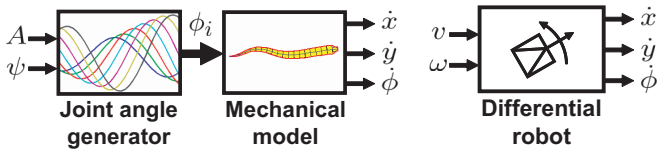

(a) (b)

Fig. 2. Model blocks of undulatory locomotion system (a) and differential-drive robot (b). In each model, (x, y, ϕ) denotes the robot head pose (first link) and the robot pose respectively. (A, ψ) plays the same role as (v, ω).

II. Modelling

In this section we briefly describe the motion equations of undulatory robotic locomotion. Then, we analyze and compare the system model with the unicycle model in order to take advantage of their similarities in the control design. Afterwards, we describe the geometry of the imaging system.

A. Modelling Undulatory Locomotion

The equations of motion of an undulatory robotic mechanism are obtained from its Lagrangian dynamics as [3]–[5], [7], [25], [26]

$$\xi = g^{-1}\dot{g} = -\mathbf{A}(r)\,\dot{r} + \mathbf{I}^{-1}(r)\,p \quad (1)$$

$$\dot{p} = ad^{*}_{\xi}\,p + f_T + f_N \quad (2)$$

$$\dot{r} = u \quad (3)$$

where $\xi = g^{-1}\dot{g}$ is the velocity of the robot's reference frame in body coordinates. The joint angle vector $r = (\phi_1, ..., \phi_{N-1})$ denotes the shape variables, with N the number of robot segments interconnected by planar revolute joints $(\phi_1, ..., \phi_{N-1})$, which are independently actuated. The matrix $\mathbf{A}(r)$ is the local form of the mechanical connection. The locked inertia tensor $\mathbf{I}(r)$ describes the total inertia of the system at shape configuration r. In (2) p is the body momentum with ad^{*}_{ξ} the infinitesimal generator of the adjoint action of the group of g onto ξ; and f_T, f_N are the external frictional forces in the tangential and normal directions of each link. In (3) we assume that the shape is fully controllable with velocity inputs of the joints u without considering the required torques. Refer to [5], [7] for details. This model is represented in Fig. 2(a) by the second block.

The motion of the robot is generated with the $N-1$ joint angle values ϕ_i as functions of time. Typically, this is achieved by generating a sinusoidal travelling body wave with a common amplitude A, frequency f, angular offset ψ and a constant phase lag ϕ_{flag} between consecutive joints [1], [2], [5]:

$$\phi_i(t) = A\sin(2\pi f t + i\,\phi_{lag}) - \psi\,,\ i = 1, ...(N-1)\,. \quad (4)$$

The angular offset ψ can be used for steering along curved paths, and it is set to $\psi = 0$ for motion in a straight line. The joint oscillation amplitude A affects the wavelength of the body wave, and the overall velocity of the system. This joint angle generation is represented in the first block of Fig. 2(a). In summary, we can relate the amplitude A with the forward velocity of the robot and the offset ψ with the steering of the robot [5]. This is quite similar to the way in which a standard mobile robot is steered, i.e. with two velocity inputs: linear velocity v and angular velocity ω. This is depicted in Fig. 2(b) with the state of the system given by (x, y, ϕ). Next, we explore this similarity in order to take advantage in the control design of the simplicity of the differential-drive robot model with respect to the undulatory robot model.

The formulation in the kinematic case refers to the case in which the kinematic constraints fully specify the dynamics in g. In the kinematic case, the momentum terms p do not exist due to symmetries of the nonholonomic constraints and the connection $\mathbf{A}(r)$ determines the motion in the full configuration space [27]. The equations of motion in the kinematic case become

$$g^{-1}\dot{g} = -\mathbf{A}(r)\,\dot{r} \quad (5)$$

$$\dot{r} = u \quad (6)$$

The state of the robot (x, y, ϕ) can be transformed to (ρ, θ, ϕ) in polar coordinates. The kinematics of a differential-drive vehicle are expressed as a function of the robot state and input velocities by

$$\begin{pmatrix} \dot{\rho} \\ \dot{\theta} \\ \dot{\phi} \end{pmatrix} = \begin{pmatrix} \cos(\phi-\theta) \\ \frac{1}{\rho}\sin(\phi-\theta) \\ 0 \end{pmatrix} v + \begin{pmatrix} 0 \\ 0 \\ 1 \end{pmatrix} \omega\,. \quad (7)$$

These previous constraints can be rewritten in terms of (5) with the connection matrix given by

$$\mathbf{A}(r) = \begin{bmatrix} 1 & 0 \\ 1 & 0 \\ 0 & 1 \end{bmatrix} \quad (8)$$

and $\dot{r} = (v, \omega)^T$, $\dot{g} = (\dot{\rho}, \dot{\theta}, \dot{\phi})^T$. It can be seen that the connection matrix is constant as the geometry of the differential-drive robot body does not vary.

We now study the system in open loop and compare graphically the models (1) and (5) by means of phase plane analysis [28]. Each phase portrait represents a family of system motion trajectories corresponding to various initial conditions. The resultant motion patterns of the system models depicted on the phase plane are shown in Fig. 3. The first row shows the phase portrait of ϕ and ρ with the differential robot model. SIMUUN simulations of the model of an undulatory robot, have been used to generate the plots of the second row. In this case, the motion of the undulatory robot is determined by the amplitude A and the offset ψ of the joint angles' control signals (4). Variables A and ψ are introduced in the plots by

$$\dot{\phi}_u = \psi\,. \quad (9)$$

$$\dot{\rho}_u = A\cos(\theta - \phi)\,. \quad (10)$$

The phase portraits of both models are superposed in the third row of Fig. 3. For this purpose, a scale factor has been applied to the ordinate axis of the phase portraits of the differential-drive robot. It can be seen that there is quite a tight fit between the phase portraits of the two models. The yawing of the undulatory robot head is clearly seen in the phase portrait ϕ, however the overall motion

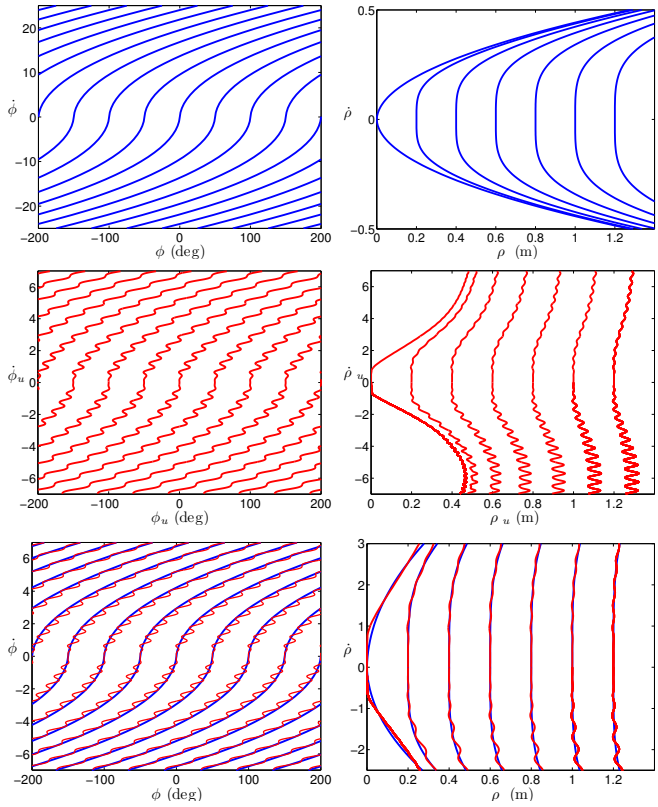

Fig. 3. Phase portrait of ϕ and ρ (Left and right column, respectively). First row refers to differential-drive model, second row refers to undulatory locomotion model and third row superposes both models with a scale factor.

characteristics are equivalent to those of the conventional robot. The superposed phase portrait ρ has been trimmed to show the phase zone with similar behavior and out of this zone the motion trajectories diverge. This is because the undulatory robotic model implemented in SIMUUN is realistic and the increasing robot velocity saturates.

We can conclude that the undulatory locomotion robot model and the differential-drive robot model (Fig. 2) demonstrate an equivalent behavior from the point of view of the input variables (A, ψ) and (v, ω). We take advantage of this equivalence in the control design of the approach presented here (although it should be noted that undulatory locomotion can exhibit richer behavior). Hereafter we denote without distinction A as v and ψ as ω.

B. Imaging geometry: The Epipoles

In our problem definition, the desired location of the robot is defined by a target image. The current and target images are related by their epipolar geometry, and this geometry is key for the development of our controller. The epipolar geometry represents the relative geometry between two views of a scene. It is independent of the scene structure and only depends on the relative configuration of the cameras and their intrinsic parameters [29]. The fundamental matrix $\mathbf{F}$, a 3×3 matrix of rank 2, is the algebraic representation of the epipolar geometry and is used to formulate the *epipolar constraint* $\mathbf{p}_2^T \mathbf{F} \mathbf{p}_1 = 0$, where $\mathbf{p}_1$ and $\mathbf{p}_2$ are any pair of

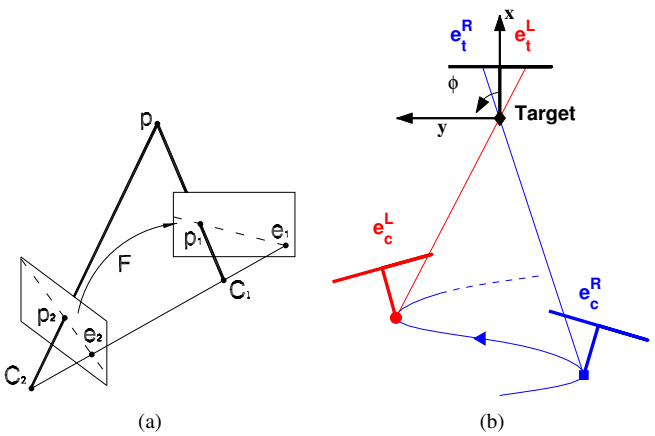

Fig. 4. (a) The epipolar geometry across two views. (b) Reference frame, with (e_c^L, e_t^L) the current and target epipoles between left current image and target image, and (e_c^R, e_t^R) between right current image and target image.

corresponding points (Fig. 4(a)). With this constraint, the fundamental matrix can be computed from a set of matched points, without knowledge of the internal camera parameters or the relative camera positions, by solving a linear system of equations [29]. The epipoles are the intersections of the baseline (the line joining the optical centers of the cameras $\mathbf{C}_1$ and $\mathbf{C}_2$) with the image planes, and they can be computed from $\mathbf{F}\mathbf{e}_1 = \mathbf{0}$ and $\mathbf{F}^T\mathbf{e}_2 = \mathbf{0}$.

A top view diagram of the robot in two particular locations and the target one at different times is depicted in Fig. 4(b), where the T-shapes represent the camera on the robot head. We consider that the robot is constrained to planar motion. Thus, the variation of the epipole vertical coordinate can be disregarded and only the horizontal coordinate of the epipoles is considered in the control design. The configuration of the camera (robot head) system is given by $(x, y, \phi)^T$, where x and y are the robot position in the plane with the origin in the target location, and ϕ is the orientation of the robot head, expressed as the angle between the robot head x-axis and the world x-axis. This is illustrated in Fig. 4(b). Polar coordinates $(\rho, \theta, \phi)^T$ are also used with θ positively measured from x-axis anticlockwise. This layout is used in the next section to develop the control design.

III. Control Scheme

In this Section we present the epipolar-based control law, and different control design issues related to the particular undulatory locomotion gait are addressed.

A. Control law

The goal is to design an image-based controller, which drives the robot to the target location defined by the target image, using directly the estimated epipoles. An overview of the visual control scheme is presented in the diagram of Fig. 5. The robot camera acquires the current images, which are used with the target image to estimate the epipolar geometry. The resultant epipoles are the input of the controller, which computes and sends to the robot the values (A, ψ) required to reach the target location. As explained later, not

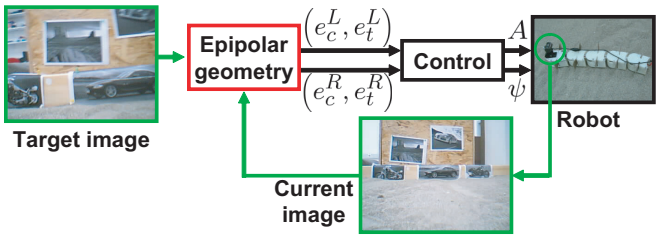

Fig. 5. Overview of the control loop.

Fig. 6. Two images acquired with the on-board camera and demonstrating the blurring effect caused by the fast head yaw during undulatory movements of the robot. The image on the left has been acquired at the limit of the head yaw, when the lateral velocity is instantaneously zero, and is therefore significantly sharper.

all the images acquired are used to estimate the epipoles, but only the particular images taken at the limits of the robot head yawing. These epipoles are denoted by L and R (Left and Right, respectively).

Conventional mobile robots perform smooth motion (in the sense that they just move forward and rotate), whereas undulatory locomotion results in a complicated motion where the robot head (and the camera) moves forward but also laterally (with a head yawing). This yawing is translated to the epipoles evolution and determines the control design. Considering a conventional robot, we could define the motion strategy correcting the robot orientation until $e_c = 0$ and moving forward keeping e_t constant. When the current epipole reaches the zero value, the robot is aligned with the baseline and the camera is pointing to the target. Thus, the robot moves forward until it reaches the target. However, this cannot be directly applied to undulatory locomotion, where the yawing motions of the head lead to an oscillatory variation of the epipoles.

Given the symmetry of the system, we can adapt the previous strategy in such a way that the robot moves toward the target when the current epipoles oscillate around the zero value. Then, an error function term can be defined based on the mean value of the current epipoles. However, there are a number of practical issues with this approach, namely (i) the fact that the fast side-to-side yawing motion of the head leads to a large number of blurred frames, which are unsuitable for estimating the epipolar geometry, and (ii) the significant computational cost involved in processing all of the acquired frames. To address these issues, the processing of only certain selected frames is proposed. More specifically, the head yaw shows higher velocity at the middle of the side to side motion, giving maximally blurred images. This yawing velocity is null during a short interval of time at the lateral limits, because of the change of direction (left to right or right to left). Images taken at these limits are not blurred and can be processed with good performance. Two images taken during one of the experiments are shown in Fig. 6, the sharp image has been taken at the limit of the yawing motion, whereas the blurred image has been taken during the side to side motion. The epipoles estimated with the current image acquired at the left side limit are denoted as left epipoles (e_c^L, e_t^L), and right epipoles those estimated at the right limit side (e_c^R, e_t^R), see Fig. 4(b).

Taking into account the previous reasoning, we define the orientation velocity ω (i.e. ψ) as a function of the left and right epipoles as

$$\omega = -k_\omega (e_c^L + e_c^R)\,, \tag{11}$$

where $k_\omega > 0$ is a constant gain. The forward velocity is defined by means of the amplitude A with a constant value. The sign of the velocity v (i.e. A) is determined taking into account the field of view constraints as follows

$$v = \begin{cases} k_v & \text{if} \quad e_t^L > e_t^R \\ -k_v & \text{if} \quad e_t^L < e_t^R \end{cases} \tag{12}$$

where $k_v > 0$ is a constant gain. When the robot is close to the target, with short baseline, the epipolar geometry is not well defined. We take advantage of this situation by checking the conditioning of the estimated epipoles. Then, the forward velocity is set to zero when instability is detected in the estimated epipoles.

B. Image Selection for Left-Right Epipoles Estimation

The frame rate of the video stream in the real experiments is 30 frames per second with image size 320×240 pixels. As mentioned earlier, not all the images can be processed in real time for the epipolar geometry estimation and not all the images are useful as many of them are blurred. Thus, only images at the left and right limits are considered for the estimation of the epipoles.

This raises the issue of accurate and efficient detection of the images corresponding to these positions from the video stream acquired by the camera. One possible approach would be to synchronize the image acquisition with the robot's control module generating the joint angles (4). This would require providing feedback from the robotic platform to the visual control system (since, as the latter requires significant computational resources, it would most likely be implemented off-board). Instead, the approach adopted here, which is described next, is aimed at keeping the visual control system as much independent of the robot as possible.

A local robust blur estimation method for image restoration has been presented in [30]. This method is very fast, performing correctly at our frame rate, and it has been adapted for our purposes. There, a blur map of the image is estimated by computing the difference ratio between the original image and its two digitally re-blurred versions. The out-of-focus blur is modelled with a Gaussian distribution in 2D, whereas

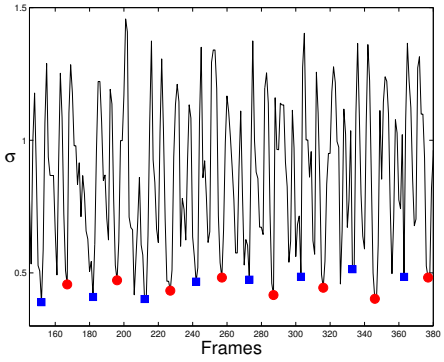

Fig. 7. Example of blur estimation along a video sequence for image selection for the control. Left and right limit images have been manually selected and depicted with circle and square markers, showing they correspond to minimum peaks.

in our control scheme the motion blur is modelled with a 1D Gaussian distribution in the image abscissa coordinate. The unknown blur radius is the standard deviation σ. The original image is re-blurred with the convolution of two Gaussian blur kernels σ_a and σ_b, with $\sigma_a < \sigma_b$. The ratio r of the differences between the original image and the two re-blurred versions is computed in every pixel. Then, local maximum ratio r_{max} is used to estimate the local blur radius σ with

$$\sigma \approx \frac{\sigma_a \, \sigma_b}{\sigma_b + (\sigma_b - \sigma_a) \, r_{max}} \, . \tag{13}$$

Refer to [30] for details. We are not interested in local blur but a global image blur metric and then, we compute the mean of the image σ values. We have tested this method with video sequences acquired by the robot. An example of the resultant σ along the frames is given in Fig. 7. The minimum peaks correspond to less blurred images, i.e. the images to be processed for the epipolar geometry estimation. To check the results we have manually selected the left and right limit images and depicted them in Fig. 7 with circle and square markers respectively. It can be seen that all these left-right images are correctly detected by lowest peaks. The robustness of the method is improved by taking into account that left and right images appear periodically, in the example of Fig. 7 with a period around 15 frames. Therefore, the periodic minimum peaks discriminate between blurred and not blurred images and allow the selection of left-right images for the epipolar geometry estimation.

IV. Controllability Analysis

In this section we study the controllability of the proposed control scheme. For this purpose we deduce the relation between the system state derivative $(\dot{\rho}, \dot{\theta}, \dot{\phi})$ with the control input derivatives $(\dot{e}_c, \dot{e}_t)$. The undulatory locomotion model has been compared with the unicycle model in Section II showing their equivalent behavior for our control purposes. Thus, we analyze the controllability of the control scheme by means of model (5). Given that the nonlinear system (5) is driftless, its controllability can be tested with the Lie Algebra rank condition (LARC) [31], [32]. Then, the system is small-time controllable if and only if the rank of the vector space spanned by the family of vector fields available to the system along with all their brackets is of full rank everywhere.

The epipoles can be related geometrically with the system state as follows [23]

$$e_c = \alpha \, \tan(\phi - \theta) \, , \tag{14}$$

$$e_t = \alpha \, \tan(\theta) \, , \tag{15}$$

where α is the focal length of the camera. The derivatives of the epipoles in matrix form give

$$\begin{pmatrix} \dot{e}_c \\ \dot{e}_t \end{pmatrix} = \alpha \begin{bmatrix} \frac{-\sin(\phi-\theta)}{\rho \cos^2(\phi-\theta)} & \frac{1}{\cos^2(\phi-\theta)} \\ \frac{\sin(\phi-\theta)}{\rho \cos^2(\theta)} & 0 \end{bmatrix} \begin{pmatrix} v \\ \omega \end{pmatrix} . \tag{16}$$

From (7) and solving for the robot velocities in (16), the kinematics equations are expressed as

$$\begin{pmatrix} \dot{\rho} \\ \dot{\theta} \\ \dot{\phi} \end{pmatrix} = \frac{1}{\alpha} \begin{bmatrix} 0 & \frac{\rho \cos^2(\theta)}{\tan(\phi-\theta)} \\ 0 & \cos^2(\theta) \\ \cos^2(\phi-\theta) & \cos^2(\theta) \end{bmatrix} \begin{pmatrix} \dot{e}_c \\ \dot{e}_t \end{pmatrix} . \tag{17}$$

Note that the matrix in (16) is singular if $(\phi - \theta) = 0, \pi$. The vector fields $\{\mathbf{f}_1, \mathbf{f}_2, [\mathbf{f}_1, \mathbf{f}_2]\}$ are then defined as

$$\mathbf{f}_1 = \begin{pmatrix} 0 & 0 & \frac{\cos^2(\phi-\theta)}{\alpha} \end{pmatrix}^T , \tag{18}$$

$$\mathbf{f}_2 = \begin{pmatrix} \frac{\rho \cos^2(\theta)}{\alpha \tan(\phi-\theta)} & \frac{\cos^2(\theta)}{\alpha} & \frac{\cos^2(\theta)}{\alpha} \end{pmatrix}^T , \tag{19}$$

$$[\mathbf{f}_1, \mathbf{f}_2] = \begin{pmatrix} \frac{-\rho \cos^2(\theta)}{\alpha^2} & 0 & 0 \end{pmatrix}^T . \tag{20}$$

The Lie Algebra rank condition is tested checking if the following determinant is not null:

$$det \, [\mathbf{f}_1 \, \mathbf{f}_2 \, [\mathbf{f}_1, \, \mathbf{f}_2]] = \rho \cos^2(\phi - \theta) \cos^4(\theta) / \alpha^4 \, . \tag{21}$$

It can be seen that the span of the vector field is full rank except at $\rho = 0$, $|\theta| = \pi/2$ or $|\phi - \theta| = \pi/2$. Therefore, the system is small-time controllable with the control scheme defined except in these cases. When $|\theta| = \pi/2$ we have that $e_t = \infty$, and $|\phi - \theta| = \pi/2$ corresponds to $e_c = \infty$. Then, any motion strategy should avoid these situations. Besides, these cases will imply that the robot loses the target out of the field of view for sure with a standard camera. The vector field loses rank with the robot in the target location $\rho = 0$, but specially in this case the short baseline problem has to be addressed. More relevant is to take into account the case when the matrix in (16) is singular $(\phi - \theta) = 0$. This condition holds when the robot moves in a straight line pointing towards the target. There, the orientation can be corrected but not the distance to the target (ρ-coordinate). But in fact, what our undulatory robot cannot do is to move in this way. Thus, because of the yawing of the robot head, the angle ϕ will oscillate between the limit values ϕ^L and ϕ^R avoiding the singularity.

V. Stability Analysis

In this section the stability of the control scheme presented is analyzed by means of *Lyapunov's Direct Method*. The robot position was expressed in polar coordinates $\mathbf{x}(t) =$

$(\rho, \theta, \phi)^T$ with the reference system depicted in Fig. 4(b). We define the Lyapunov candidate function as

$$V(\mathbf{x}, t) = V_\rho + V_\theta + V_\phi = \frac{(e_\rho)^2}{2} + \frac{(e_\theta)^2}{2} + \frac{(e_\phi)^2}{2} \ , \quad (22)$$

with $e_\rho = (\rho - \rho^d)$, $e_\theta = (\theta - \theta^d)$ and $e_\phi = (e_c^L + e_c^R)$. The values ρ^d and θ^d denote the desired values and $(e_c^L + e_c^R)$ represents the angular error in terms of the epipoles.

This candidate function is positive definite given that $V(\mathbf{x}) > 0$ for all $\mathbf{x} \neq \mathbf{x}^d$ and $V(\mathbf{x}^d) = 0$. Now we analyze the derivative Lyapunov candidate function of each term to show it is strictly negative. After differentiating we obtain: $\dot{V} = \dot{V}_\rho + \dot{V}_\theta + \dot{V}_\phi$ where

$$\dot{V}_\rho = e_\rho \, \dot{e}_\rho = (\rho - \rho^d) \, \cos(\phi - \theta) \, v \ . \quad (23)$$

$$\dot{V}_\theta = e_\theta \, \dot{e}_\theta = (\theta - \theta^d) \, \sin(\phi - \theta) \, v / \rho \ . \quad (24)$$

$$\dot{V}_\phi = e_\phi \, \dot{e}_\phi = (e_c^L + e_c^R)(\dot{e}_c^L + \dot{e}_c^R) \ . \quad (25)$$

Each term is now studied to show that $\dot{V}$ is negative. The desired location of the homing task is $\rho^d = 0$ and $\theta^d = \theta$, then $\dot{V}_\rho = \rho \, \cos(\phi - \theta) \, v$ and $\dot{V}_\theta = 0$. Given that $\rho > 0$ we need to check that

$$sign(v) \neq sign(\cos(\phi - \theta)) \ , \quad (26)$$

If the robot is behind the target then $\cos(\phi - \theta) > 0$ and the robot moves forward with $v > 0$ (12). Otherwise, if the robot is in front of the target with $\cos(\phi - \theta) < 0$, we have that the robot moves backward with $v < 0$. This assumption is due to the field of view constraints $|\theta| > |\phi|$. The error ϕ of the closed loop is represented by

$$\dot{e}_\phi + k_\omega \, e_\phi = 0 \, , \quad (27)$$

and the control law (11) has been defined as

$$\omega = -k_\omega \, e_\phi \, , \quad (28)$$

and then $\dot{V}_\phi < 0$. Therefore, the control law of the system is locally stable in the Lyapunov sense. The stability analysis assumes that the epipolar geometry is properly estimated and therefore the system is constrained in such a way that enough features can be matched across the images without short baseline. This constraint limits to local stability, which consequently depends on the field of view of the camera and the scene.

VI. Simulations and Experiments

This section presents simulation results validating the proposed control scheme, and describes the setup employed for preliminary experimental investigations.

A. Simulation Results

The proposed visual control method has been implemented and validated in the SIMUUN simulation environment [24], developed at ICS-FORTH. SIMUUN is based on the SimMechanics toolbox of Simulink® and provides tools for modelling the body mechanics, the interaction with the environment and the shape control of undulatory systems. The visual control simulations presented here employ a model of an eel-shaped 20-link undulatory mechanism, which has been created in SIMUUN. A quadratic friction force model is used for the interaction of the mechanism's links with the environment (for details, see [24]).

Results obtained from the simulations are shown in Fig. 8. In the example of the first row the robot performs a straight line path toward the target. Another example is given in the second row in which the robot moves in a curve to reach the target location. The resultant paths obtained are shown in Fig. 8(a) together with the target location, depicted with a diamond marker, and it can be seen that the robot reaches in both cases the target location. The orientation of the robot head (and, hence, the orientation of the camera) is shown in Fig. 8(b). The evolution of the estimated epipoles is shown in Fig. 8(c), where the left (e_c^L) and right (e_c^R) epipoles computed at the yaw limits are drawn with circular and square markers respectively. In the example of straight motion, the temporal evolution of the epipoles' location can be seen to oscillate around zero, as would be expected. In the second example, the curved path evolves, in response to the epipoles' oscillation gradually converging to a zero mean value. At the end of the motion, when the robot is close to the target location, the epipoles become unstable as can be seen in the plot of the estimated epipoles. Finally, temporal evolution of the control signals ψ and A, shaping the undulatory wave of the system during navigation to the target location, is shown in Fig. 8(d).

A virtual scene has been created using the Persistence of Vision Ray-Tracer (POV-Ray^{TM}). The virtual scene is rendered and projected into the image plane through a pinhole camera model. A sequence of virtual images taken during the navigation in SIMUUN is shown as example in the **video** attachment.

B. Experiments

The experimental setup for testing the proposed scheme is presented in this section. It employs the Nereisbot prototype [6], which is a 5-segment robotic platform developed at ICS-FORTH for studying undulatory locomotion as well as pedundulatory extensions thereof, where body undulations are combined with appropriately synchronized movements of leg-like appendages (termed parapodia). Nereisbot can be adapted for locomotion over a wide variety of substrates, both conventional (e.g., hard floors) and unstructured (e.g., sand, pebbles and grass). In the present study, locomotion over sand is considered, where the body undulations may be complemented by parapodial activity. The robot has been fitted with a forward-looking camera (Sweex WC031), connected to a host PC via USB. In the proposed setup (currently not fully implemented), the host PC processes in real-time the images acquired by the camera, computes the control law and sends the corresponding controls (A, ψ) to the robot, via a wireless link.

Images are acquired by the on-board camera at 30 frames per second with a resolution of 320×240 pixels. The resolution selected provides a balanced compromise between computation time and accuracy of the geometric model esti-

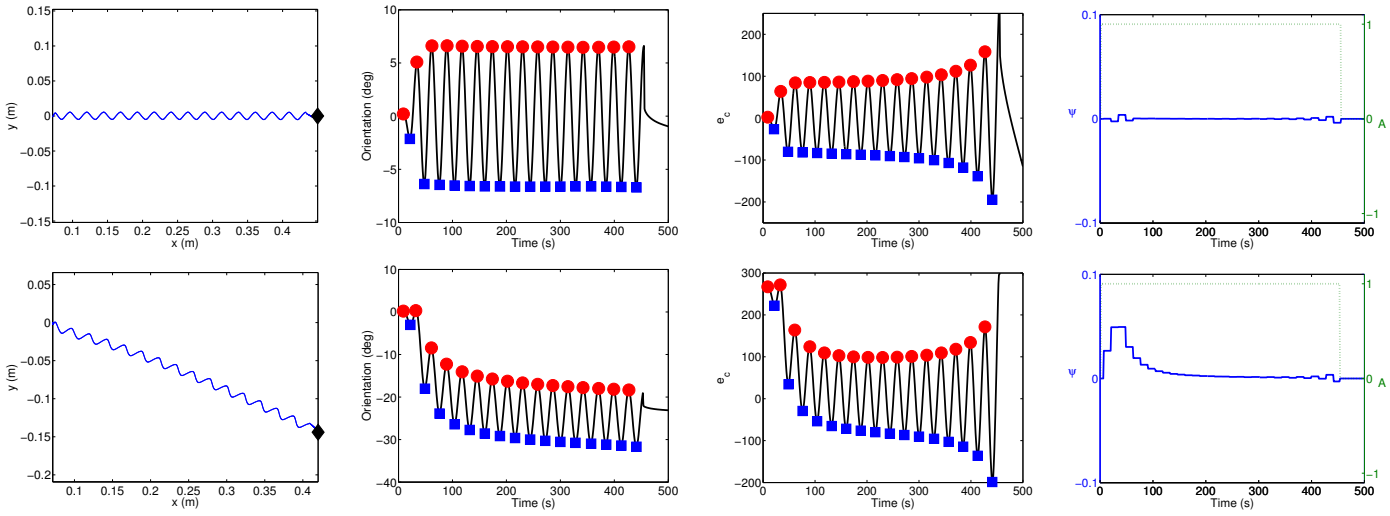

(a) Path (x, y) (b) Head orientation (ϕ) (c) Current epipoles (e_c) (d) Control output (ψ, A)

Fig. 8. Results of two simulations in which the robot follows a straight path to reach the target (first row) or a curve path (second row). The target location is drawn with a diamond marker. (c) The left and right current epipoles (e_c^L, e_c^R) are depicted with circular and square markers respectively.

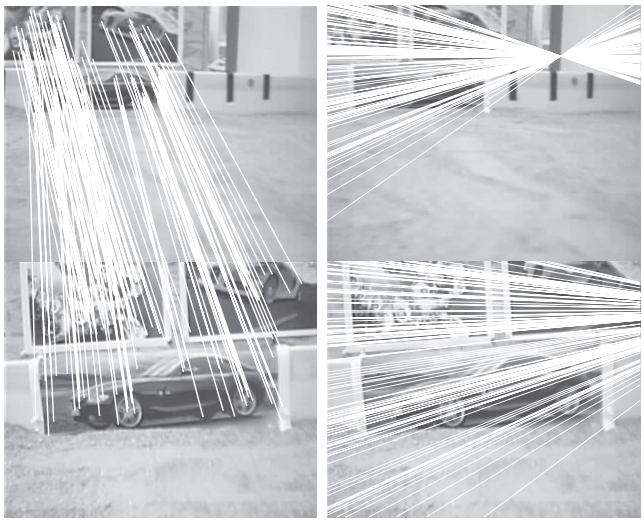

Fig. 9. SIFT matches between a current and a target image (left). Epipolar lines intersecting on the epipoles estimated (right).

mations. The epipolar geometry is computed between current and target images where the current images (left or right) are selected following the procedure outlined in Section III-B. Then, SIFT features [33] are extracted and matched between the current and the target images. An example of the matches and the epipolar geometry obtained between a current and a target image is shown in Fig. 9. The epipoles are estimated using the RANSAC method [29], which is robust to the presence of outliers. The estimation of the epipolar geometry is programmed using OpenCV (Intel® Open Source Computer Vision Library). The estimated epipoles are used as input to the control law, which calculates the corresponding values of A and ψ.

Two real experiments are presented as a proof of concept in Fig. 10. These experiments have been carried out in open loop, thus, the robot is controlled to move in an arbitrary path: a straight line in the first example and a curve in the second. The video sequence of images is grabbed during the navigation and one of the last images is selected as target image. Then, the video is processed off-line estimating the epipoles and computing the output of the control law. The values obtained for A and ψ are consistent with the motion performed in open loop. In the control design we use only the horizontal coordinate of the epipoles assuming planar motion. The coordinates of the epipoles are depicted in Fig. 10 showing variation in the vertical coordinate. In practice, this variation can be disregarded with respect to the horizontal coordinate variation. Figure 11 shows the robot in the target location for the curve path experiment from a external camera. The trajectory of the camera during the movement of the robot is indicated in white. An example with real data is shown in the **video** attachment.

VII. Conclusion

A novel visual homing scheme for undulatory robots has been presented, where the control law is defined in terms of epipoles. The adopted image-based approach does not require computing the robot's position or extracting depth or other 3D scene information. Adaptations coping with features specific to undulatory locomotion have been introduced, especially with respect to the fast yawing movements of the mechanism's head link. The feasibility of the proposed scheme has been demonstrated through simulations and preliminary experiments with a robotic platform. Apart from homing, this control scheme could also be applied to tracking (where a moving object is defined as the target). Work is currently underway toward performing in-depth parametric simulation studies, and developing real-time implementations for the closed-loop experimental validation.

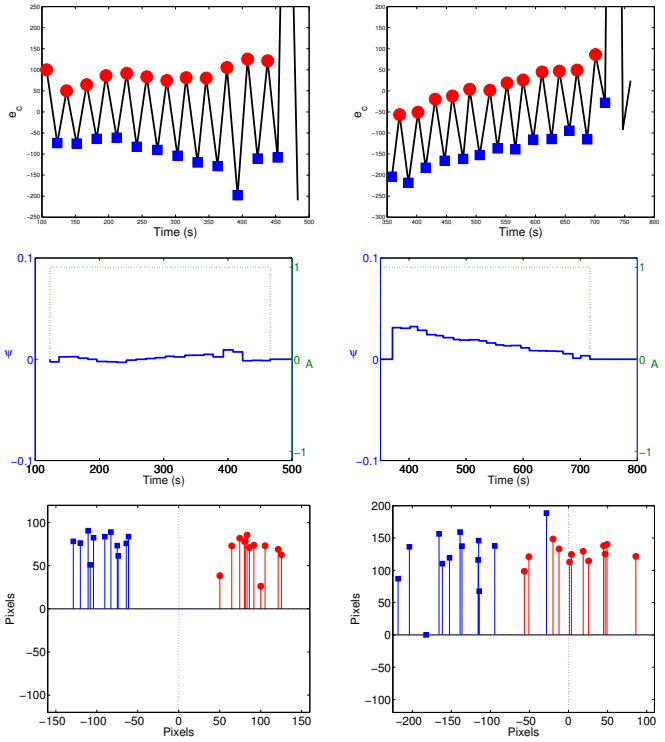

Fig. 10. Two experiments with real data in open loop in which the robot follows a straight line to reach the target (left column) or a curve (right column). 1^{st} row: Current epipoles (e_c^L, e_c^R) depicted with circular and square markers, respectively. 2^{nd} row: Control output (ψ, A). 3^{rd} row: Coordinates in the image plane of the current epipoles along the motion.

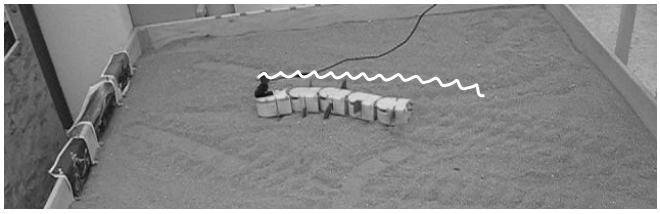

Fig. 11. Path followed by the camera in the second experiment of Fig. 10.

REFERENCES

[1] J. Ostrowski and J. Burdick, "The geometric mechanics of undulatory robotic locomotion," *International Journal of Robotics Research*, vol. 17, pp. 683–701, 1998.

[2] S. Hirose, *Biologically Inspired Robots: Snake-like Locomotors and Manipulators*. Oxford University Press, 1993.

[3] J. Cortes, S. Martinez, J. P. Ostrowski, and K. A. McIsaac, "Optimal gaits for dynamic robotic locomotion," *The International Journal of Robotics Research*, vol. 20, no. 9, pp. 707–728, 2001.

[4] P. Krishnaprasad and D. P. Tsakiris, "Oscillations, SE(2)-snakes and motion control: a study of the roller racer," *International Journal of Dynamical Systems*, vol. 16, no. 4, pp. 347–397, 2001.

[5] G. La Spina, M. Sfakiotakis, D. Tsakiris, A. Menciassi, and P. Dario, "Polychaete-like undulatory robotic locomotion in unstructured substrates," *IEEE Transactions on Robotics*, vol. 23, no. 6, pp. 1200–1212, Dec. 2007.

[6] M. Sfakiotakis and D. P. Tsakiris, "Undulatory and pedundulatory robotic locomotion via direct and retrograde body waves," in *IEEE International Conference on Robotics and Automation*, 12–17 May 2009 (to appear).

[7] ——, "Biomimetic centering for undulatory robots," *International Journal of Robotics Research*, vol. 26, no. 11-12, pp. 1267–1282, 2007.

[8] B. Klaassen and K. Paap, "GMD-SNAKE2: a snake-like robot driven by wheels and a method for motion control," in *IEEE International Conference on Robotics and Automation*, vol. 4, 1999, pp. 3014–3019.

[9] M. Kolesnik and H. Streich, "Visual orientation and motion control of makro - adaptation to the sewer environment," in *Proceedings 7th Int. Conference on Simulation of Adaptive Behavior*, 2002, pp. 62–69.

[10] G. Kulali, M. Gevher, A. Erkmen, and I. Erkmen, "Intelligent gait synthesizer for serpentine robots," in *IEEE International Conference on Robotics and Automation*, vol. 2, 2002, pp. 1513–1518.

[11] R. Worst and R. Linnemann, "Construction and operation of a snake-like robot," in *IEEE International Joint Symposia on Intelligence and Systems*, Nov 1996, pp. 164–169.

[12] G. N. DeSouza and A. C. Kak, "Vision for mobile robot navigation: A survey," *IEEE Transactions on Pattern Analysis and Machine Intelligence*, vol. 24, no. 2, pp. 237–267, 2002.

[13] Y. Ma, J. Kosecká, and S. Sastry, "Vision guided navigation for a nonholonomic mobile robot," in *Proceedings of the 36th IEEE CDC San Diego, CA*, 1996, pp. 3069–3074.

[14] D. P. Tsakiris, C. Samson, and P. Rives, "Extending visual servoing techniques to nonholonomic mobile robots," in *The Confluence of Vision and Control*, ser. Lecture Notes in Control and Information Systems (LNCIS), D. K. G. Hager and S. Morse, Eds. Springer-Verlag, 1998, vol. 237, pp. 106–117.

[15] A. A. Argyros, K. E. Bekris, S. C. Orphanoudakis, and L. E. Kavraki, "Robot homing by exploiting panoramic vision," *Autonomous Robots*, vol. 19, no. 1, pp. 7–25, 2005.

[16] R. Basri, E. Rivlin, and I. Shimshoni, "Visual homing: Surfing on the epipoles," *International Journal of Computer Vision*, vol. 33, no. 2, pp. 117–137, 1999.

[17] S. Benhimane, E. Malis, P. Rives, and J. R. Azinheira, "Vision-based control for car platooning using homography decomposition," in *IEEE International Conference on Robotics and Automation*, April 2005, pp. 2173–2178.

[18] E. Malis, F. Chaumette, and S. Boudet, "2 1/2 D visual servoing," *IEEE Transactions on Robotics and Automation*, vol. 15, no. 2, pp. 234–246, Apr. 1999.

[19] A. Argyros, D. Tsakiris, and C. Groyer, "Biomimetic centering behaviour for mobile robots with panoramic sensors," *IEEE Robotics and Automation Magazine, special issue on Panoramic Robotics*, vol. 11, no. 4, pp. 21–30, Dec. 2004.

[20] Y. Fang, W. E. Dixon, D. M. Dawson, and P. Chawda, "Homography-based visual servo regulation of mobile robots," *IEEE Transactions on Systems, Man, and Cybernetics, Part B*, vol. 35, no. 5, pp. 1041–1050, 2005.

[21] P. Rives, "Visual servoing based on epipolar geometry," in *IEEE/RSJ International Conference on Intelligent Robots and Systems*, vol. 1, 2000, pp. 602–607.

[22] G. L. Mariottini, D. Prattichizzo, and G. Oriolo, "Epipole-based visual servoing for nonholonomic mobile robots," *IEEE International Conference on Robotics and Automation*, pp. 497–503, 2004.

[23] G. López-Nicolás, C. Sagüés, J. J. Guerrero, D. Kragic, and P. Jensfelt, "Switching visual control based on epipoles for mobile robots," *Robotics and Autonomous Systems*, vol. 56, no. 7, pp. 592–603, 2008.

[24] M. Sfakiotakis and D. Tsakiris, "SIMUUN: A simulation environment for undulatory locomotion," *International Journal of Modelling and Simulation*, vol. 26, no. 4, pp. 4430–4464, 2006.

[25] R. M. Murray, "Nonlinear control of mechanical systems: A lagrangian perspective," in *Annual Reviews in Control*, vol. 21, 1997, pp. 31–45.

[26] A. M. Bloch, *Nonholonomic Mechanics and Control*. Berlin: Springer-Verlag, 2003.

[27] S. D. Kelly and R. M. Murray, "Geometric phases and robotic locomotion," *J. Robotic Systems*, vol. 12, no. 6, pp. 417–431, 1995.

[28] J.-J. E. Slotine and W. Li, *Applied nonlinear control*. Prentice Hall, Englewood Cliffs NJ, 1991.

[29] R. I. Hartley and A. Zisserman, *Multiple View Geometry in Computer Vision*, 2nd ed. Cambridge University Press, 2004.

[30] H. Hu and G. de Haan, "Adaptive image restoration based on local robust blur estimation," in *Lecture Notes on Computer Science (ACIVS)*, 2007, pp. 461–472.

[31] A. Isidori, *Nonlinear Control Systems*. Springer, 1995.

[32] S. M. LaValle, *Planning Algorithms*. Cambridge University Press (also available at http://msl.cs.uiuc.edu/planning/), 2006.

[33] D. Lowe, "Distinctive image features from scale-invariant keypoints," *Int. Journal of Computer Vision*, vol. 60, no. 2, pp. 91–110, 2004.